How to cite: *Angew. Chem. Int. Ed.* **2024**, *63*, e202406497
doi.org/10.1002/anie.202406497

Helical Nanographenes | Hot Paper

Nonalternant B,N-Embedded Helical Nanographenes Containing Azepines: Programmable Synthesis, Responsive Chiroptical Properties and Spontaneous Resolution into a Single-Handed Helix

*Weiwen Zhuang, Faan-Fung Hung, Chi-Ming Che, and Junzhi Liu**

Abstract: Heteroatom-embedded helical nanographenes (NGs) constitute an important and appealing class of intrinsically chiral materials. In this work, a series of B,N-embedded helical NGs (BN-HNGs) bearing azepines was synthesized via stepwise regioselective cyclodehydrogenation. First, the phenyl- or nitrogen-bridged dimers were efficiently clipped into highly congested model compounds **1** and **2**. Later, the controllable Scholl reactions of the tetraphenyl-tethered precursor generated 1, 7 or 8 new C–C bonds, thereby establishing a robust method for the preparation of nonalternant BN-HNGs with up to 31 fused rings. The helical bilayer nature was unambiguously verified by X-ray diffraction analysis. The helical chirality was transferred to the stereogenic boron centers upon fluoride coordination, with a concave-concave structure to comply with the bilayer skeleton. Notably, the largest nonalternant BN-HNG (**6**) spontaneously resolved into a homochiral 4_1 helix structure as a molecular spiral staircase during crystallization via conglomerate formation at the single-crystal scale. The large twisted C_2-symmetric π-surface and the dynamic chiral skeleton induced by curved azepines might have synergistic effects on self-recognition of enantiomers of **6** to achieve the intriguing spontaneous resolution behavior. The chiroptical properties of the enantiomer of **6** were further investigated, revealing that **6** had a strong chiroptical response in the visible range (400–700 nm).

[*] W. Zhuang, F.-F. Hung, Prof. Dr. C.-M. Che, Dr. J. Liu
State Key Laboratory of Synthetic Chemistry, HKU-CAS Joint Laboratory on New Materials and Department of Chemistry
The University of Hong Kong
Pokfulam Road, Hong Kong, 999077, P.R. China
E-mail: juliu@hku.hk

Dr. J. Liu
Materials Innovation Institute for Life Sciences and Energy (MILES), HKU-SIRI
Shenzhen, 518005, P.R. China

Introduction

Helical nanographenes (HNGs), as cutouts of graphene with smaller honeycomb lattice structures consisting of sp^2-hybridized carbon atoms, have garnered significant interest due to their distinct dynamic behaviors and chiroptical properties.[1] Tailored chiroptical properties and high stereochemical stability of HNGs are desirable for their potential applications in the fields of circularly polarized light (CPL)-based materials, such as 3D displays, optical switches, and chiral sensors.[2,3]

The geometries and electronic structures of nanographenes are judiciously altered by nonalternant topologies.[4] Notably, the configurational stability of HNGs, including those with heptagonal,[5] octagonal,[6] and nonagonal[7] rings, was significantly enhanced by negative curvatures. Therefore, the controllable integration of negatively curved units via the straightforward Scholl reaction is important for streamlined synthesis.[8] Furthermore, the dynamic conformational changes induced by negative curvatures enrich morphologies spanning from the nanoscale to mesoscopic scale. The resulting assembly behavior of HNGs plays a pivotal role in transforming the inherent molecular properties into supramolecular functionalities.[9] For example, recently, Qiu et al. reported the impressive assembly behavior of π-extended diaza[7]helicene with two negatively curved azepines,[10] in which homochiral lamellae of the 23-ring fused triple helicene could be obtained by spontaneous resolution, whereas the phenomena were serendipitously reported for simpler helicenes.[11]

Recent works have suggested that the introduction of boron-nitrogen (B,N) atoms into helical polycyclic conjugated hydrocarbons (PCHs) could improve the circular dichroism (CD) and CPL performance.[12] And the azepination of B,N-embedded skeletons is beneficial for efficient emitters.[13] However, as the number of *ortho*-fused rings increased, the accumulated strain and steric hindrance between the fledged side arms impeded facile synthesis and backbone modification of B,N-embedded HNGs (BN-HNGs) containing [n]helicene units ($n>7$).[14] Thus far, an efficient approach to construct diverse higher BN-HNGs containing negatively curved azepines remains elusive, which hinders determination of the correlation between the structure, assembly behaviors, and chiroptical properties within this appealing chiral molecular family. In addition, transfer of chiral information during the preparation of helical NGs is attractive yet challenging,[15] and the stereo-

specific coordination of tridentate boron atoms would provide an alternative pathway to tune the chiroptical properties of the as-synthesized BN-HNGs.

Herein, we report a modular and programmable approach to construct a novel class of nonalternant B,N-embedded HNGs (**1**–**6**) bearing azepine units via selective Scholl reactions (Figure 1). The structure-dependent packing in the solid state,[16] photophysical and electrochemical properties, and responsive chiroptical properties were systematically studied. The chirality transfer process from BN-HNGs to the corresponding boron-stereogenic derivatives upon fluoride coordination was established. Interestingly, the large twisted C_2-symmetric π-surface and the dynamic chiral skeleton induced by the curved azepines might have the synergistic effects on self-recognition of enantiomers of **6** to achieve the intriguing spontaneous resolution behavior.

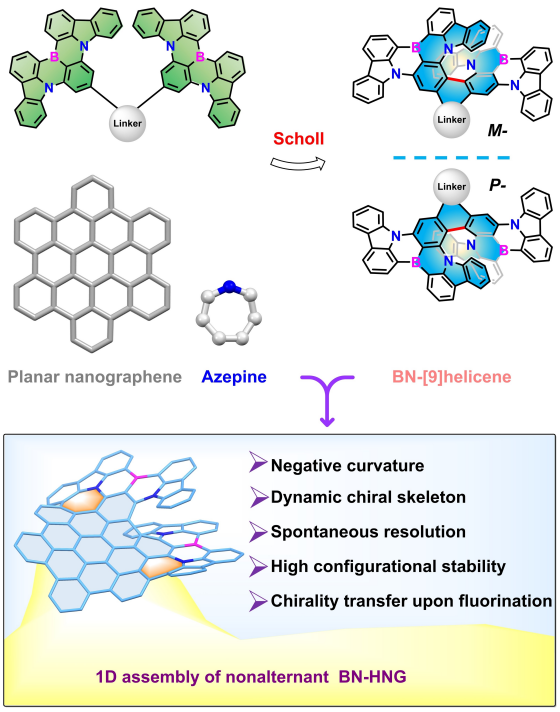

Figure 1. Design concept of nonalternant B,N-embedded helical nanographenes with azepines produced via a selective Scholl reaction.

Results and Discussion

Synthesis of Model Compounds 1 and 2

As depicted in Scheme 1a, the synthesis of model compound **1** with 20 fused rings started from tetrafluoroterphenyl **7** in 3 steps. Sequential introduction of iodine atoms and 3,6-di-*tert*-butyl-1-carbazoles (*t*BuCz) was conducted with a total yield of 86 % without purification of the iodinated intermediate. This twofold one-pot borylation of **8** afforded the desired precursor **9** in 36 % yield. An intramolecular Scholl reaction between two multi-resonance (MR) cores of **9** in the presence of iron (III) chloride ($FeCl_3$) in a mixed solvent of dichloromethane (DCM) and nitromethane provided **1** as an orange-red powder at the gram scale in 72 % yield. Notably, the Suzuki–Miyaura cross-coupling reaction between 1,2-diiodobenzene and CzBN-Bpin,[12g] which is a widely utilized linchpin for efficient construction of multi-resonance MR molecules, failed to yield precursor **9** (Figure S1). Although unexpected aryl migration or rearrangement reactions occasionally occurred during the Scholl reaction in some circumstances with large steric hindrance,[17] to our delight, mild Scholl reaction conditions under the $FeCl_3$/DCM/$MeNO_2$ combination afforded **1** with exceptionally high regioselectivity and efficiency.

To our surprise, replacement of the phenyl linker by arylamine via a Pd-catalyzed twofold Buchwald–Hartwig amination reaction with readily synthesized compound **10**,

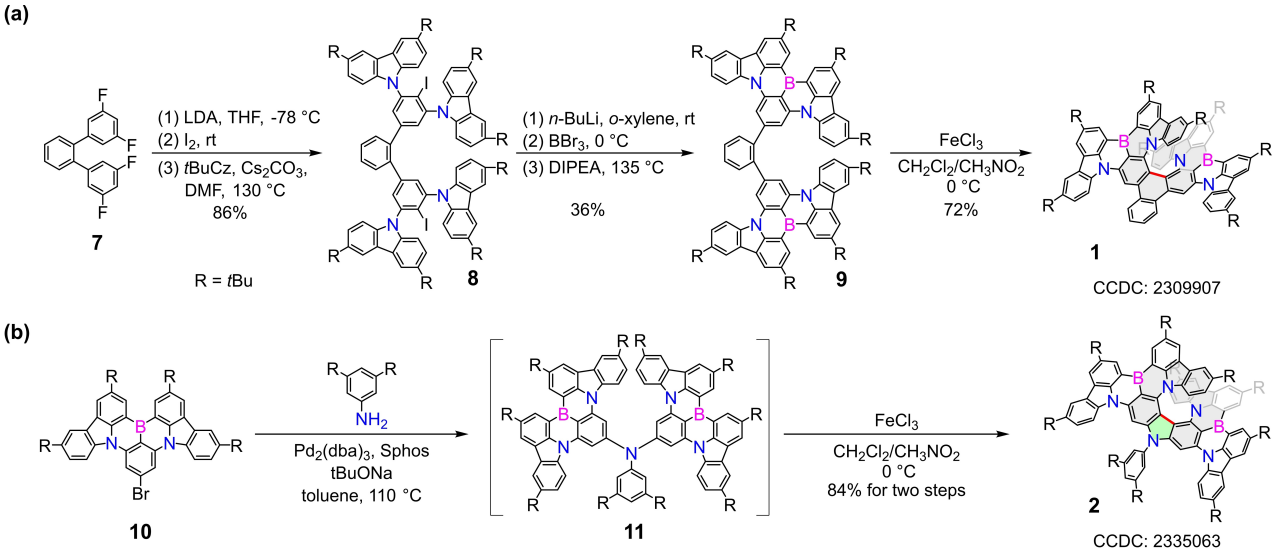

Scheme 1. Synthesis of model compounds **1** (a) and **2** (b).

afforded precursor **11**, which underwent an $FeCl_3$ mediated Scholl reaction to generate nitrogen-rich boron-embedded [9]helicene (**2**) in 84 % yield in two steps (Scheme 1b). The straightforward gram-scale synthesis of **2** via oxidative cyclodehydrogenation provided a brand-new pathway for efficient pentagon generation of helical carbazole motifs, avoiding the high loading of palladium catalysts in the intramolecular C–H/C–H coupling.[18]

Structural Elucidation of Model Compounds 1 and 2

The highly congested structure of **1** was elucidated by a combination of NMR spectroscopy, high-resolution mass spectrometry and single crystal x-ray diffraction (SC-XRD) (Figures 2b and S16a). To verify the hypothesis of transfer of the chiral information of [9]helicene to the prochiral tridentate boron upon reversible coordination of Lewis bases, such as fluoride anions, *tetra-n*-butylammonium fluoride (TBAF) or boron trifluoride diethyl etherate ($BF_3{\cdot}OEt_2$) was selected as the additives (Figure 2a). Upon the addition of TBAF, the intensities of the absorption peaks at 413, 500 and 550 nm gradually decreased (Figure 2c). A new peak appeared at 525 nm and reached the highest intensity with 0.9 eq. TBAF, which could be assigned to the one-fluoride intermediate. Further addition of TBAF (up to 5.4 eq.) led to the disappearance of the 525 nm peak

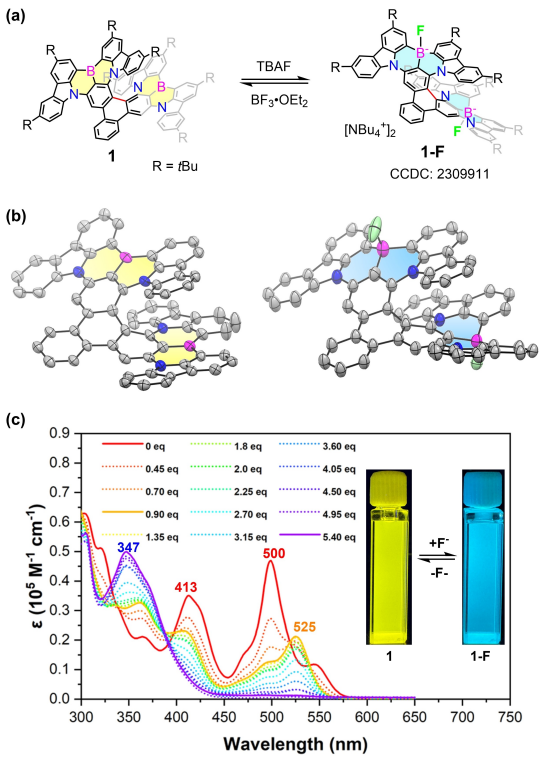

Figure 2. Reversible coordination of fluoride with **1** (a). Crystal structures of **1** (b, left) and **1-F** (b, right). Hydrogen atoms and *tert*-butyl groups were omitted for clarity. Titration of **1** with TBAF monitored by UV–Vis absorption spectroscopy in THF (10^{-5} M) (c). The inset shows the graph under 365 nm UV light.

and the evolution of a broad peak at 300–400 nm owing to dianion species (**1-F**). The resulting **1-F** solution had a sky-blue emission under 365 nm UV light. When excess $BF_3{\cdot}OEt_2$ was added to the mixture, regeneration of **1** was observed, along with a color change under 365 nm UV light (inset graph of Figure 2c). In situ ^{1}H NMR characterization of **1-F** was conducted in THF-d_8, which showed shielded signals in the aromatic region after the addition of TBAF (~5 eq.) (Figure S2). The clear NMR signal also indicated a highly symmetric structure of **1-F** with two chiral borate ions comprising a C,C,C,F-tetradentate $(C_3BF)^-$ backbone.

A crystal of difluorinated adduct **1-F** was obtained with 7.0 equivalents of TBAF (in THF) by slow diffusion of methanol into a toluene solution. The structural variation between **1** and **1-F** was shown in Figure 2b. Importantly, the chiral information of the helicity was smoothly transferred to the central chirality of the $(C_3BF)^-$ subunit, generating a pair of enantiomers, namely, (S_B, M_{9H}, S_B)/(R_B, P_{9H}, R_B)-**1-F** (Figure S16). The subscript letter (B or 9H) indicates the borate center or the [9]helicene moiety, and the letter (*S* or *R*; *P* or *M*) indicates the chirality of the corresponding moiety. The stereogenic borate centers of **1-F** were quite different from the achiral (N_2BF_2) unit of BODIPY,[19] the achiral $(N_2CBF)^-$ borate of double [5]helicene,[20] or various chiral borates of $(O_4B)^-$, $(N_2CBF)^-$, $(CNOBF)^-$, $(CNO_2B)^-$, *etc.*[21] The *quasi*-planar geometry of the boron atoms of **1** was distorted by the coordination of fluoride. However, the overall helicity of the [9]helicene core did not substantially change, as indicated by the similar centroid-centroid distances between the pentagons of the inner circuits, which were 3.283 and 3.232 Å for **1** and **1-F**, respectively (Figure S21). The trigonal orientation of the boron atoms in **1** decreased after fluoride coordination, adopting a tetrahedral geometry, which stretched the carbazole motifs of the outer wings outward, affording a convex-convex structure. The convex-convex structure was attributed to the intramolecular steric hindrance of the two NBN-layers, which inhibited the coordination of fluoride in the inner circuit, namely, *re*-faces of *M*-enantiomer and *si*-faces of *P*-enantiomer. This conclusion was further supported by density-functional theory (DFT) calculations, which indicated that the concave-concave (1.9 kcal/mol) and concave-convex (0.5 kcal/mol) structures had higher Gibbs free energies than the convex-convex (0 kcal/mol) structure (Figure S60a). The nonaromatic character of ring E did not substantially change after fluoride complexation, as indicated by nucleus-independent chemical shifts (NICS) values (Figure S60b). The formation of strong B–F bond could compensate for the nonaromatic characteristics of rings G and C in **1-F**. For instance, ring G of **1-F** showed a larger positive NICS(0) value (4.2) than that of **1** (1.2). On the other hand, the generation of BF_4^- anion in the presence of $BF_3{\cdot}OEt_2$ could make the conversion of **1-F** to **1** energetically favorable, which was also supported by the shorter B–F bonds of BF_4^- (~1.36 Å) than that of **1-F** (~1.47 Å).[22] The optimized concave-concave structure had a bowl depth of 1.46 Å, which could increase to 2.54 Å in the concave-convex structure. In contrast, shallow convex regions were found in the solid state of **1-F**. In addition, the distance between the

concave fluoride and the nearest intramolecular *tert*-butyl group of the optimized structures was around 3.1 Å, indicating steric repulsion. Interestingly, compressed heterochiral columnar packing along the *b*-axis of **1** was identified, with a pitch of approximately 1.5 nm (Figure S16a); while**1-F** adopted a loose alternative layered 1D-columnar packing mode with a pitch length along the *c*-axis of 2.6 nm (Figure S16b). Fluorinated dianions with opposite configurations were separated by layers consisting of two *tetra-n*-butylammonium groups with short C–H···F contacts between the ammonium cation and fluoride anion of 2.32–2.67 Å (red circles in Figure S16b).

The nitrogen-rich boron-embedded [9]helicene (**2**) was also verified by crystallographic analysis (Figure 3a). The undeviating C_2-symmetric bilayer structure had compact stacking of intramolecular and intermolecular NBN-blades, with plane-to-plane distances of 3.70 and 3.46 Å, respectively. Compared to **1**, the nitrogen-linked analog showed a narrowed and blueshifted emission band centered at 520 nm, which is promising for pure-green CPL emitter (Figure 3b). There was no obvious change in the absorption and emission spectra in various solvents with different polarities, indicating a marginal intramolecular charge-transfer character (Figure S26). **2** has five nitrogen atoms, and five reversible oxidative peaks were found in the cyclic voltammetry (CV) and differential pulse voltammetry (DPV) curves (Figure 3c). The first oxidative peak at 0.16 eV (vs. Fc*/Fc*$^+$, Fc*: decamethylferrocene) indicates the electron-rich nature of **2**, which prompted us to investigate the possibility of generating charge-transfer or electron-donor-acceptor (EDA) complexes with various electron acceptors. The mixtures of **2** and a series of electron acceptors were monitored by ^{1}H NMR (Figures S13–15). 1,2,4,5-Tetracyanobenzene (**TCNB**) and tetracyanoquinodimethane (**TCNQ**) showed shielded proton signals after the addition of **2** in $CDCl_3$, while **2** was unaffected. On the other hand, 2,3-dichloro-5,6-dicyano-1,4-benzoquinone (DDQ) and *p*-chloranil resulted in broadening peaks of **2**. However, the absorption and luminescence spectra showed minimal changes after the addition of the electron acceptor (Figures S26 and S27). Fortunately, the planar electron acceptor **TCNB** was co-crystalized with **2** and toluene at a molecular ratio of 1/1/1 by slow diffusion of methanol into the corresponding solution (**2/TCNB** = 1/1.2) (Figure 3d). The columnar alternative stacking of the *P*/*M*-enantiomers was interrupted by two kinds of repeating **TCNB** layers, adopting a B-A-B'-A-B packing mode. The distances between the **TCNB** and NBN-layers were determined to be 3.45–3.51 Å, while the distance between the intramolecular NBN-layers exhibited a marginal change after co-assembly. The remaining multiple resonant structures of **1** and **2** were further elucidated by the distribution of frontier molecular

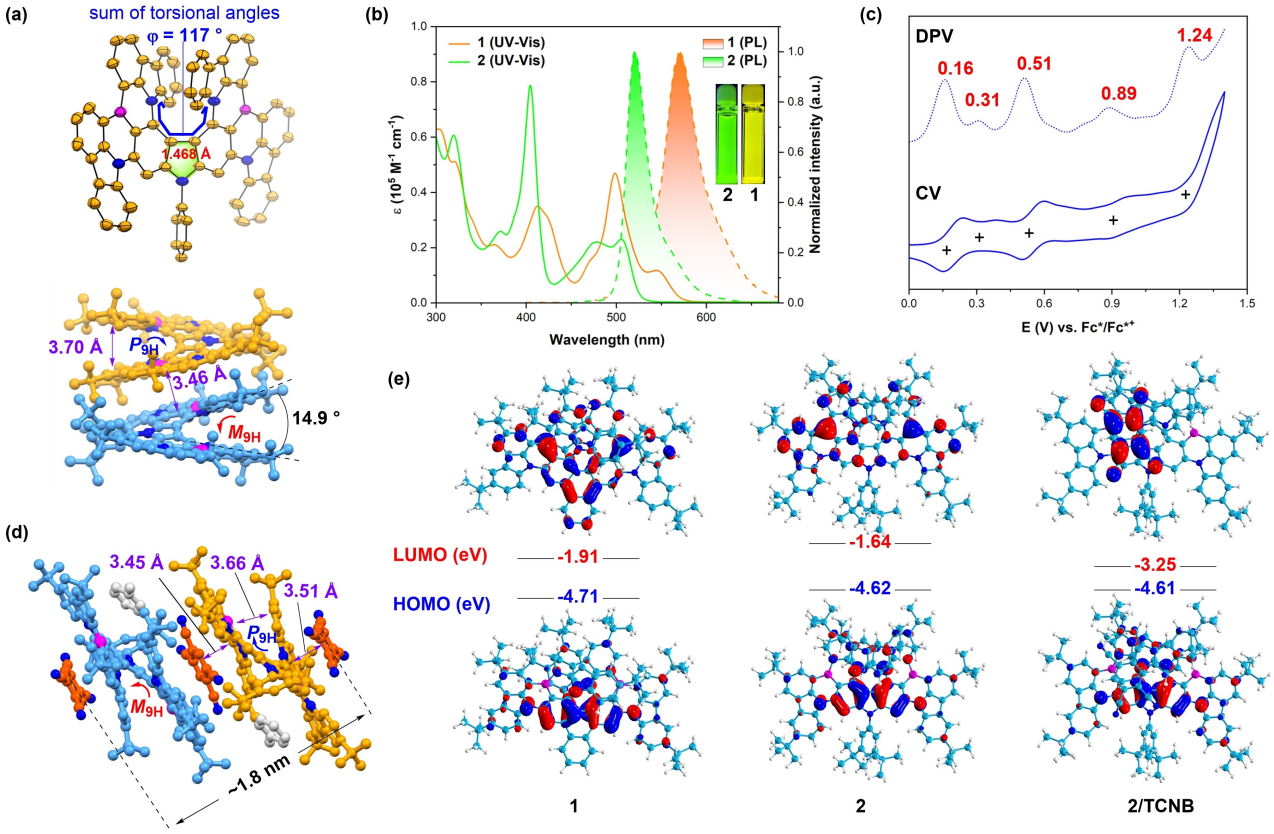

Figure 3. Crystal analysis of **2** (a). UV–Vis absorption and emission spectra of **1** and **2** in toluene (10^{-5} M) (b); the inset shows the graph under 365 nm UV light. CV and DPV curves of **2** in dichloromethane (10^{-3} M) (c). Cocrystal of **2** and **TCNB** (d). Carbon atoms of (*P*)-**2**, (*M*)-**2**, toluene and **TCNB** were colored in orange, blue, gray and red, respectively. Calculated frontier molecular orbitals of **1**, **2** and **2**/**TCNB**, isovalue = 0.03 (e).

orbitals at B3LYP-D3(BJ)/6-31G(d) level of theory (Figure 3e). The highest occupied molecular orbitals (HOMO) of **1** and **2** were found to be located at similar positions regardless of the bridge. However, **2** had a higher-lying lowest unoccupied molecular orbital (LUMO) of −1.64 eV and a larger HOMO–LUMO gap (2.98 vs. 2.80 eV) owing to the electron-donating arylamine unit. On the other hand, DFT calculations based on the obtained crystal of **2/TCNB** suggested that the HOMO and LUMO were located on **2** and **TCNB**, respectively. Therefore, **2/TCNB** is a good candidate for applications of EDA complexes in the fields of photoredox catalysis and organic field-effect transistors (OFETs).[23]

Synthesis of Laterally π-Extended BN-HNGs via Stepwise Scholl Reactions

The highly efficient cyclodehydrogenation reaction and the protruding edge of **1** provided an easy access to lateral π-extension. The hexaarylbenzene precursors **14a/b** with two adjacent MR-cores and four additional phenyls were prepared via Diels–Alder cycloaddition between alkyne **12** and 2,3,4,5-tetraarylcyclopenta-2,4-dien-1-ones **13a/b** (Scheme 2). Compound **10** coupling with ethynyltrimethylsilane via the palladium/copper-catalyzed Sonogashira reaction afforded **12** in moderate yield (51 % for two C–C bonds). This one-pot twofold Sonogashira reaction without isolation of the presumable TMS-protected intermediate was reported previously.[24] Water and 1,8-diazabicyclo-[5.4.0]undec-7-ene (DBU) might promote the removal of TMS-group to facilitate the second C–C coupling. An electron-donating methoxy group was introduced at the *para*-position to facilitate the Scholl reaction. However, treatment of **14a** in DCM with $FeCl_3$/nitromethane at 0 °C or room temperature (rt) gave only the major product **4** as a pink solid with a set of asymmetric ^1H NMR signals and a characteristic ^{13}C NMR peak at 186.6 ppm (Figure S81). The formation of the spirocyclic dienone motif was further verified by SC-XRD (Figure 4b). Similarly, when **14a** was subjected to the Scholl reaction with DDQ/triflic acid (HOTf) in DCM at 0 °C, **4** was obtained in 66 % yield. On the other hand, the reaction of **14a** and $FeCl_3$/nitromethane in highly diluted DCM at 0 °C for 3 minutes gave only the monocyclized product (**3a**) in 62 % yield (35 % of **14a** was recovered). The newly generated C–C bond between the adjacent MR-cores resulted in a highly distorted [9]helicene core of **3a** (Figure 4a). Further oxidative dehydrogenation

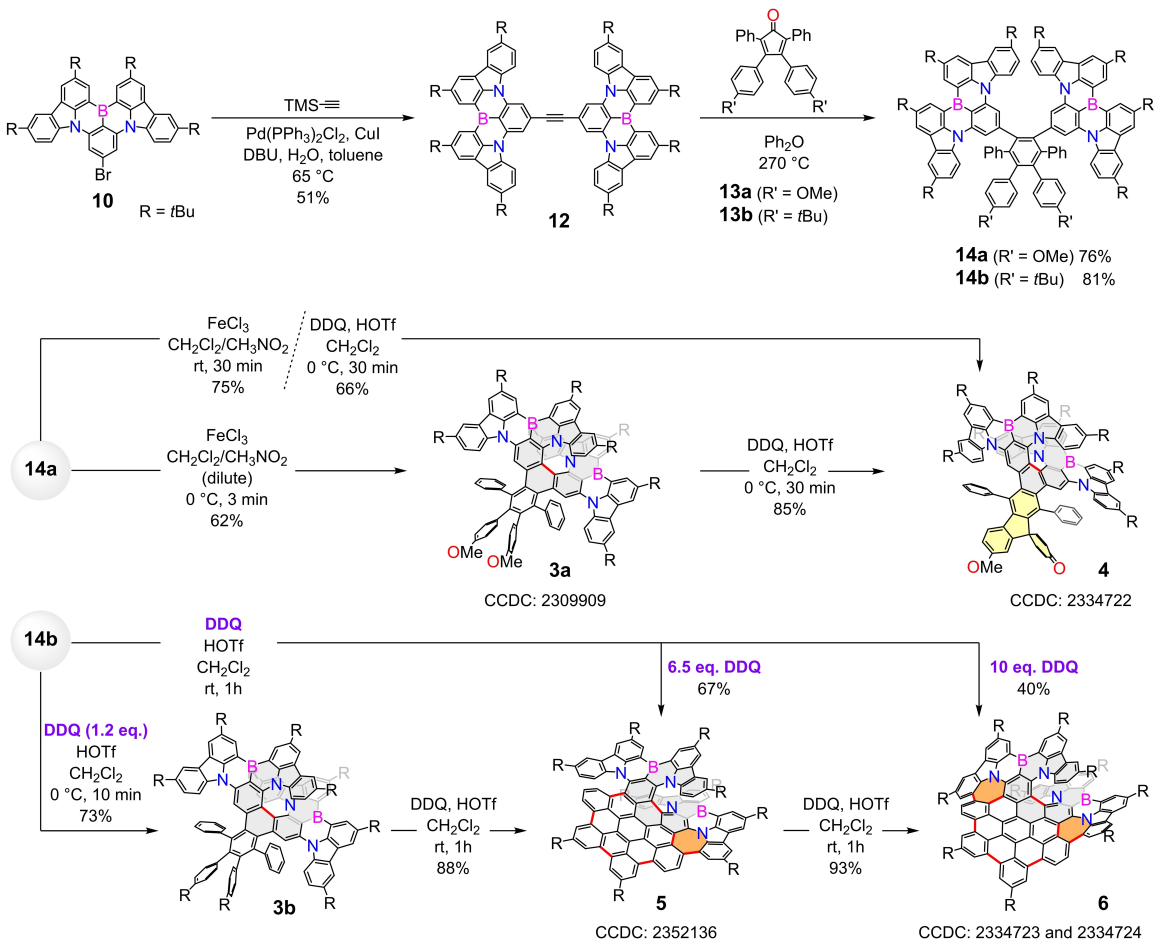

Scheme 2. Synthesis of laterally π-extended BN-HNGs via stepwise Scholl reactions.

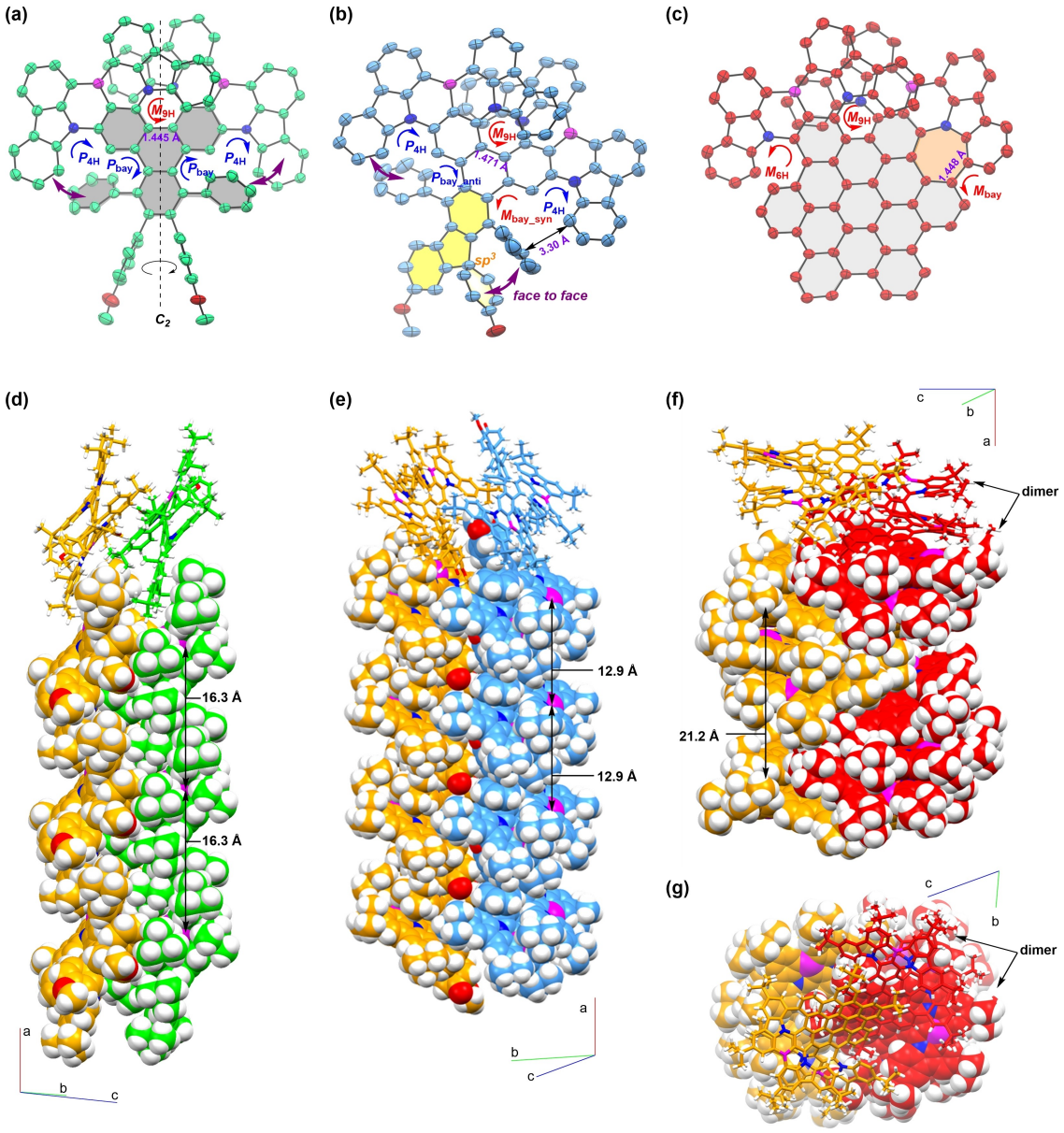

Figure 4. Crystal structures of **3a** (a, d) **4** (b, e), and **5** (c, f, g). Carbon atoms of *P*-enantiomers are colored in orange. Carbon atoms of *M*-enantiomers of **3a**, **4** and **5** were colored in green, blue and red, respectively. Hydrogen atoms and *tert*-butyl groups were omitted for clarity (a-c). Toluene was omitted for clarity (f, g).

reaction of racemic **3a** under DDQ/HOTf conditions led to the demethylation and formation of a spirocyclic motif (**4**) in 85 % yield. Further Scholl cyclization of **4** was attempted, but no new spots were generated. The sequential transformations with favored cyclization between MR-cores indicated electronic properties for cyclodehydrogenation.

The exceptionally high selectivity of the first Scholl cyclization, which afforded [9]helicene core of **3a**, prompted us to theoretically investigate the reaction process. Generally, Scholl reactions involve two possible mechanisms, namely, arenium cation pathway and radical cation pathway. Previous reports have indicated that $FeCl_3$-mediated cyclodehydrogenative cyclization likely processeds via radical cation intermediates.[25] Thus, when **14a** was oxidized by $FeCl_3$, the generated radical cation showed significant spin density at the *meta*-positions of the boron atoms in both MR-blades (Figure S61a), which is in good agreement with the experimental results. On the other hand, a strong protonic acid (HOTf) would be feasible for an arenium cation intermediate. The Mulliken charges of **14a** at the *ortho*-positions of nitrogen atoms in the core are −0.220, −0.228, −0.212, and −0.214, indicating a greater tendency for protonation at these positions (Figure S61b). The sequential transformation of **3a** was proposed to proceed via a methoxyl-activated demethyl-cyclization pathway following the literature precedents.[26]

When the removable methoxy peripheries were replaced by *tert*-butyl (*t*Bu) groups to generate **14b**, the following

Scholl reaction under mild conditions afforded the monocyclized product **3b** with high efficiency and excellent selectivity. In contrast to **14a**, the $FeCl_3$/nitromethane system at rt with **14b** gave only **3b** without further fusion of other aryl groups, which was also validated by the comparison of ^{1}H NMR spectra of **3a** and **3b** (Figure S4). Interestingly, when an excess amount of DDQ (8.0 eq.) was used as the oxidant, the use of methanesulfonic acid (MSA) as the Brønsted acid at rt promoted only a one-fold Scholl reaction and gave **3b** in 70 % yield. Treatment of **14b** with different equivalents of DDQ in a mixed solvent of DCM and HOTf at rt afforded laterally π-extended derivatives of **1** (**5** and **6**), which were firstly confirmed by high-resolution matrix-assisted laser desorption/ionization time-of-flight (MALDI-TOF) mass spectrometry. With 1.2 eq. DDQ at 0 °C, **3b** could be quickly generated within 10 minutes in 73 % isolated yield. When the reaction temperature was increased to rt and the mixture was stirred for 1 hour, two major spots (**5** and **6**) were isolated in the presence of 8.0 eq. DDQ, corresponding to dark purple powders. The product with a greater polarity (**5**) exhibited a set of unsymmetrical ^{1}H NMR signals, indicating asymmetric π-extension of **3b** and loss of the C_2-symmetric axis (Figures S5–9). Further cyclodehydrogenation of **5** by DDQ/HOTf could afforded **6** with an additional azepine unit. The nonalternant topologies of **5** and **6** were unambiguously verified by SC-XRD (Figures 4c and 5a). The yields of **5** and **6** were further improved to 67 % (6.5 eq. DDQ) and 40 % (10.0 eq. DDQ), respectively.

Structural Characterization of BN-HNGs

High-quality single crystals of **3a**, **4**, **5**, and **6** were obtained by slow diffusion of methanol into their toluene solutions at ambient temperature in the dark. Crystallographic analysis revealed that π-π interactions were enhanced by larger π-conjugation. As depicted in Figure 4a, the MR-blades and the uncyclized phenyl groups of **3a** in the bay region of the central triphenylene (filled in gray) adopted an X-shaped orientation owing to the steric repulsion. Thus, a novel axially chiral nonplanar triphenylene subunit was introduced. Owing to the relatively low racemization barriers of highly flexible nitrogen-centered [4]helicene subunits, the dynamic behavior of such structures in solution is envisioned to be barrierless. Depending on the helicity of the [9]helicene moiety and the axial chirality of the substituted bay regions, **3a** might have 6 possible stereoisomers, (P_{bay}, P_{9H}, P_{bay})/(M_{bay}, M_{9H}, M_{bay}), (P_{bay}, P_{9H}, M_{bay})/(M_{bay}, M_{9H}, P_{bay}), and (P_{bay}, M_{9H}, P_{bay})/(M_{bay}, P_{9H}, M_{bay}). The subscript letter (9H or bay) indicates the [9]helicene moiety or axially chiral bay region, and the letter (*P* or *M*) indicates the chirality of the corresponding moiety. The obtained **3a** was determined to be a racemic mixture of (P_{bay}, M_{9H}, P_{bay}) (green) and (M_{bay}, P_{9H}, M_{bay}) (orange) in a single crystal (Figure 4d). The helicity of [9]helicene is opposite to those of bay regions and [4]helicenes. The tilted herringbone packing of the same conformers had a long distance (16.3 Å) between two adjacent molecules.

Although the skeleton of **4** was expanded by spirofluorene, the chirality still arose from the central [9]helicene motif, which was unequivocally established by SC-XRD (Figures 4b and 4e). The as-synthesized *spiro*-fused BN-HNG molecule consisted of a racemic mixture of (*M*)/(P)-**4**, which was further supported by chiral high-performance liquid chromatography (HPLC) resolution (Figure S47). Unlike **3a**, the spiro-dienone cycle forced the phenyl group on the same side to be oriented in a face-to-face direction, deforming the helicity of the bay region to M_{bay_syn} (Figure 4b). The C··· centroid distance between the carbon atom of carbazole and the perpendicular bay phenyl ring was measured to be 3.30 Å. The newly generated C–C bond in the [9]helicene subunit of **4** was 1.471 Å, which is longer than that of **3a** (1.445 Å), indicating a single bond character. Interestingly, as an extended derivative of model compound **1**, **4** adopted a slightly slipped herringbone packing mode with homochiral columns, which could be ascribed to reduced π-π interactions between enantiomers resulting from the larger π-surface and increased steric hindrance induced by the surrounding pendants. The pitch length for three stacked molecules of **1** was approximately 1.5 nm (Figure S16a), and a larger value of 2.6 nm was found for **4**, as the distance between two adjacent **4** molecules was 1.3 nm (Figure 4e).

The [6]- and [9]helicene moieties of **5** adopted the same helicity of azepine-associated bay region (Figure 4c). A racemic mixture of (P_{6H}, P_{9H}, P_{bay})/(M_{6H}, M_{9H}, M_{bay})-**5** was found in the solid state (Figures 4f and 4 g). The columnar stack is composed by alternatively arranged dimers of the same configuration. And a shorter pitch length (21.2 Å) was found. Compared to uncyclized analogues **3a** and **4**, the fused hexa-*peri*-benzocoronene (HBC)-unit of **5** showed strong intermolecular π-π interactions (Figure 4g). The negative curvature induced by azepine was found to assist the twisted packing of homochiral dimer (Figure S19).

Enantiomeric enrichment was found during the crystallization of racemic **6**, and spontaneous resolution was achieved at the single-crystal scale. The overall distorted chiral skeleton of **6** with a C_2-symmetric axis is depicted in Figure 5a. The introduction of [9]helicene and azepines deformed the hexagonal rings of HBC (rings D–K). The sum of torsion angles of [9]helicene unit is 192°, which is larger than those of **1** (140°) and **2** (117°), presumably due to the formation of heptagonal rings. The bay region of azepine adopted the same helicity as [9]helicene, with a dihedral angle of 31.9°. The resulting wavy HBC core had a cooperative dynamic structure with complementary concave-convex regions. The dynamic nature of twisted HBC was also confirmed by concentration-dependent ^{1}H NMR spectroscopy (Figures 5c and S12). When the concentration in CD_2Cl_2 at rt increased from 1 mM to 8 mM, upfield shifts of proton resonances (h-m) were observed, which indicated self-aggregation of **6** in solution. The unchanged signals of protons (c-g) were ascribed to the rigidity of the azepine-locked side-arm. Intense and continuous intramolecular and intermolecular π-π interactions between fledged NBN-blades were identified in the solid state, which was further elucidated by Hirshfeld partition (IGMH) analysis[27] (Fig-

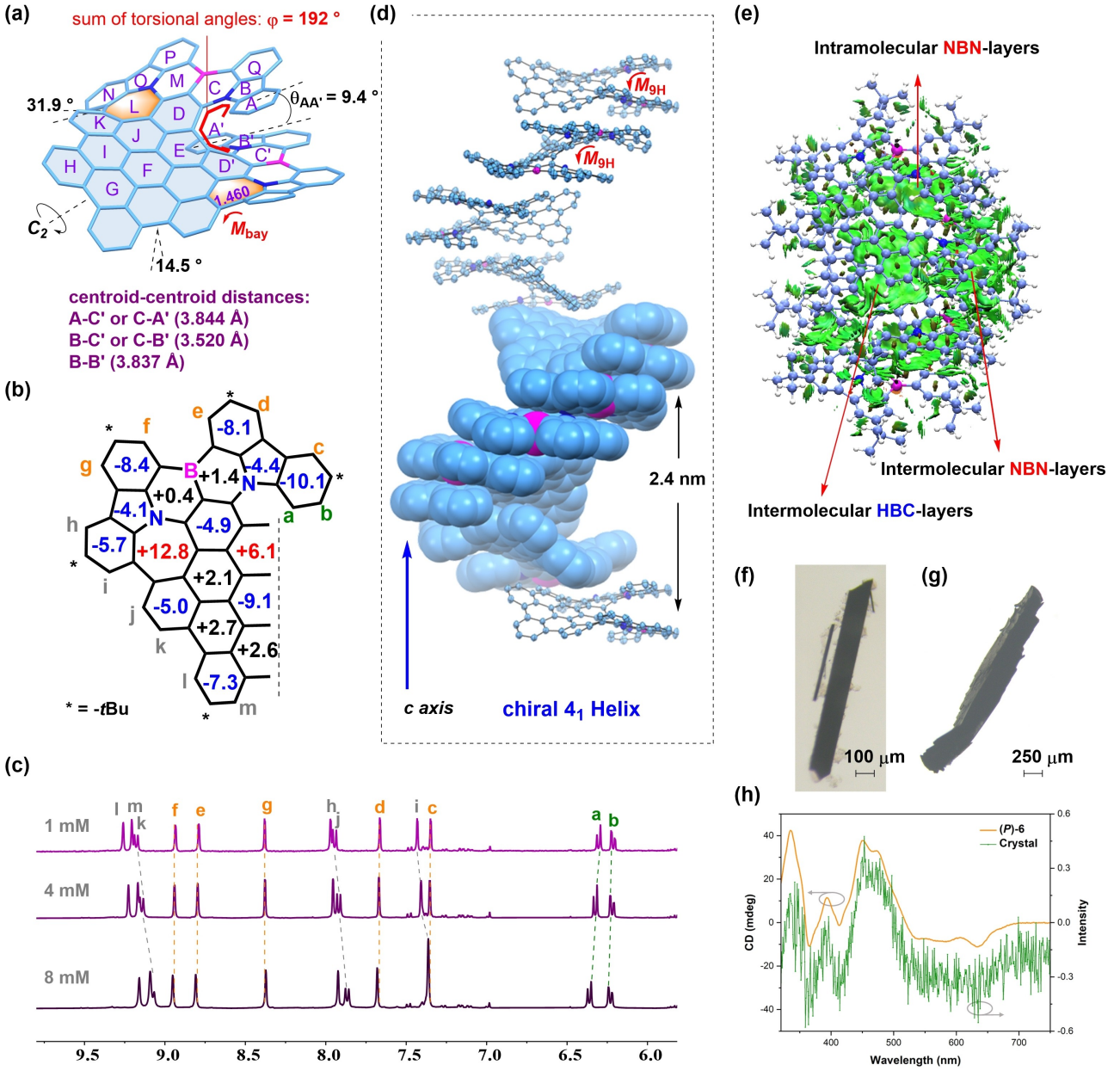

Figure 5. Crystal structures of **6** (a and d). Only one enantiomer was observed due to spontaneous resolution into the non-centro-symmetric $C222_1$ space group. Absolute stereochemistry was not determined from the data and the asymmetric units of *M*-enantiomers were tentatively shown in light blue. Hydrogen atoms and *tert*-butyl groups were omitted for clarity. NICS(0) values of **6** (b). Variable-concentration ^{1}H NMR spectra of **6** in CD_2Cl_2 at 298 K (c). Hirshfeld partition (IGMH) analysis of dimeric **6**, with the noncovalent interactions indicated by green surfaces (e). Crystal of **6** obtained by slow diffusion of methanol into a chlorobenzene solution (f). Crystal (g) and the corresponding CD spectrum in toluene (h) of **6** obtained by slow diffusion of methanol into a toluene solution of racemic **6**.

ure 5e). Overall, the peculiarity of the molecular topology and stacking of **6** became apparent; when viewed along the *c* axis or perpendicular to the central ring E, a molecular spiral staircase was identified (Figure 5d). The complementary filling of curved HBCs by each other in the inner circuit facilitated the formation of a conglomerate, which was also supported by the shielded proton resonance signals upon condensation. Tracking downward along the stairs, the chiral helix led to an opposite handedness of the enantiomeric **6** molecule, namely, (*P*)-helix from (*M*)-**6**. The 4_1 helix contained 4 molecules of **6** per helical turn, with a twisted angle of 90° between adjacent molecules. The pitch of the molecular spiral staircase was determined to be around 2.4 nm. Each helix was surrounded by six homochiral columns with the same configuration that meshed in the single crystals. Therefore, helical voids were formed between the helices, which adopted the same handedness as the molecular spiral staircases (Figures S24 and S25).

Notably, spontaneous resolution of racemic **6** into homochiral crystals was observed under two conditions:

slow diffusion of acetonitrile into a chlorobenzene solution (needle-shaped dark brown crystals, Figures 4f and S22), and slow diffusion of methanol into a toluene solution (rod-shaped black crystals, Figures 4g and S22), respectively. The absolute configuration of enantiomer forming the corresponding homochiral 4_1 helices could not be determined based on the unsatisfactory Flack parameters (Table S8). However, the spontaneous optical resolution was easy to repeat, and the crystals obtained from the methanol/toluene conditions were redissolved in toluene to record the CD spectrum. As depicted in Figure 5h, the obtained solution of the crystal from racemic **6** exhibited a similar Cotton effect pattern to that of the enantiomerically pure *P*-enantiomer (>98% ee), indicating that the obtained crystal contained enriched (*P*)-**6** and a single-handed 4_1 helix with *M*-helicity.

Photophysical and Chiroptical Properties of BN-HNGs

The stepwise cyclodehydrogenation afforded BN-HNGs with various degrees of π-extension, which not only differed from the stacking in the solid states but also altered the photophysical properties. The UV–Vis absorption (Figure 6a) and fluorescence (Figure 6b) spectra of **14b** and the resulting BN-HNGs were recorded in toluene. The precursor **14b** featured an intense absorption peak at 470 nm, assigned to the HOMO→LUMO transition. The π-extended skeleton of one-bond closed product **3b** induced redshifted absorption and emission peaks. The maximum absorption peak of **3b** at 555 nm from $S_0 \rightarrow S_1$ transition (oscillator strength $f = 0.117$) showed a lower intensity than the peak at 508 nm from $S_0 \rightarrow S_2$ transition ($f = 0.522$). The maximum absorption peaks of **5** and **6** were further redshifted to 631 and 635 nm, respectively, owing to the larger π-systems. Accordingly, the emission peaks of BN-HNGs with HBC subunit were redshifted, accompanied by azepines enabled by Scholl reaction for **5** and **6** (Figure 6b). As π-extended derivatives of **3b**, HBC-containing BN-HNGs had decreased quantum yields and no delayed fluorescence (Table 1), demonstrating the profound effect of HBC. Furthermore, the fluorescence lifetimes were measured to be 9.5, 6.9 and 6.0 ns for **3b**, **5**, and **6**, respectively.

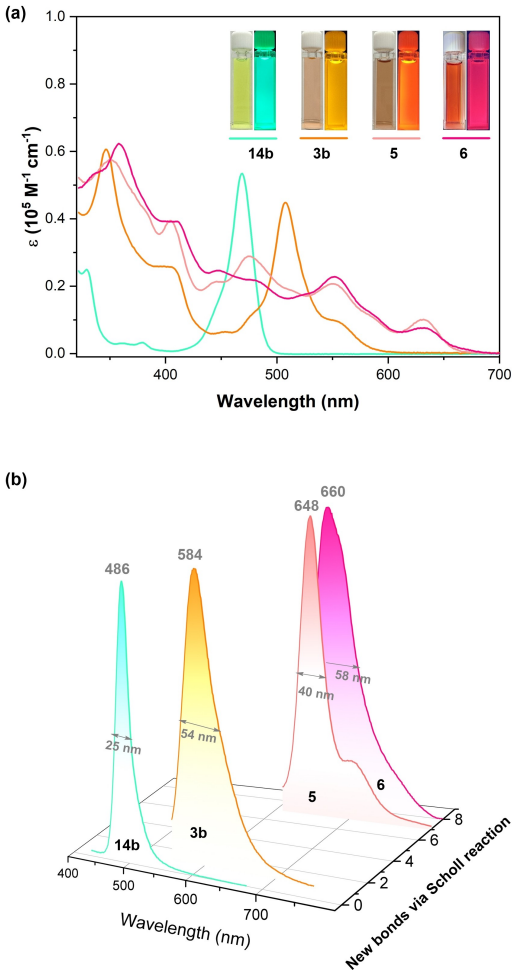

Figure 6. Photophysical properties of BN-HNGs obtained via stepwise Scholl reactions of **14b**. UV–Vis absorption (a) and normalized fluorescence (b) spectra in toluene (10^{-5} M). The inset shows the graph under day light (left) and 365 nm UV light (right), respectively.

In addition, the TBAF titration experiments indicated that BN-HNGs (**2**, **3a**, **3b**, **4**, **5** and **6**) also had obvious anion-responsive colorimetric blueshift (Figures S30–34). The titration curves of **5** and **6** showed a similar pattern. It is worth noting that a peak centered at 525 nm evolved and

Table 1: Summary of the optical and electrochemical properties of BN-HNGs.

Sample	λ_{abs} (nm)[a]	λ_{max}^{em}(nm)[a]	ν_a-ν_f (cm^{-1})[a]	FWHM (nm/eV)[a]	Φ_{PL} (%)[b]	Φ_{PL} (%)[c]	τ_F (ns)[d]	τ_{DF} (μs)[e]	E_{gap}^{opt} (eV)[f]	E_{HOMO} (eV)[g]
1	413, 500, 550	574	760	45/0.17	28	78	8.4	63.0	2.16	−5.56
1-F*	347	482	5990	71/0.37	5	6	4.1	–	2.92	–
2	404, 477, 506	520	530	27/0.12	29	88	4.9	10.2	2.17	−4.96
3a	350, 507, 552	584	990	54/0.19	28	51	9.5	78.7	2.10	−5.39
3b	346, 508, 555	584	894	54/0.19	32	68	9.5	117.6	2.12	−5.45
4	351, 516, 571	600	846	60/0.20	30	48	13.5	126.4	2.05	−5.05
5	475, 550, 631	648	415	40/0.12	19	23	6.9	–	1.88	−5.31
6	552, 635	660	600	58/0.16	18	22	6.0	–	1.87	−5.47

[a]Measured in a toluene solution (~1×10^{-5} M). [b]Quantum yield of photoluminescence (Φ_{PL}) obtained using the absolute method before N_2 bubbling. [c]Φ_{PL} after N_2 bubbling. [d]Prompt fluorescence lifetime. [e]Delayed fluorescence lifetime. [f]Optical energy gap calculated based on the onset of absorption in toluene solutions according to E_{gap}^{opt} (eV) = (1240/λ_{onset}). [g]Estimated by the oxidation peaks in dichloromethane and calculated according to $E_{HOMO} = -(4.8 + E^{ox})$ eV. *Measured in THF.

then diminished during the titration experiment of **1**. In contrast, the new peak around 540 nm of **3a/b** and **4** didn't disappear even after adding 5.0 eq. TBAF. And no new peaks was found in the range of 450–550 nm for the titration of **2**. These results indicated that π-extension had strong effects on the coordination ability of boron centers and the absorption properties of the whole molecules.

The electrochemical properties of **14b** and the resulting BN-HNGs were investigated by CV and DPV. According to the CV and DPV curves (Figure S45), **14b** had an oxidation wave at 1.115 eV (vs. Fc*/Fc*$^{+}$), whereas two obvious reversable oxidation waves ($E^{ox}_{1/2}$) in the range of 0.508–0.939 eV were found for the resulting BN-HNGs. The oxidation potentials of **3b** and **5** gradually decreased with the formation of more C–C bonds. Accordingly, the HOMO levels of these two BN-HNGs were estimated to be −5.45 and −5.31 eV, respectively. Interestingly, compared to **5**, **6** had a lower HOMO level of −5.47 eV. The additional [6]helicene unit of **5** might contribute to this phenomenon.[28] Upon fluoride coordination of **6**, the HOMO level of the corresponding difluoride adduct (**6-F**) increased to −5.22 eV. The optical and chemical properties of BN-HNGs examined in this study are summarized in Table 1.

Owing to the inherent chiral [9]helicenes of the resulting BN-HNGs, high configurational stabilities of the enantiomers were envisioned. Fortunately, the enantiomers of **3b**, **4** and **6** were successfully obtained by chiral HPLC resolution (Figures S46–48). The chiroptical properties of the obtained enantiomers of **3b** (Figure 7a), **4** (Figure 7b), and **6** (Figure 7c) were evaluated by CD and CPL spectroscopy in toluene. The absolute configuration of chiral HPLC fractions was determined by comparison of the experimental CD spectra with time-dependent DFT (TD-DFT) calculations (Figure S40). A series of mirror-image Cotton effects were found. The absorption dissymmetry factors (g_{abs}) of $S_0 \rightarrow S_1$ transitions were similar for the three pairs of enantiomers (~0.004, Figures S49–51), which were the maximum g_{abs} values for **3b** and **4**. The maximum g_{abs} for **6** appeared at 450 nm for $S_0 \rightarrow S_{10}$ transition. Enantiomeric **6** had strong CD signals in the visible range (400–700 nm). The CPL spectra showed that **3b** and **4** had similar luminescence dissymmetry factor (g_{lum}) values of 0.005 (Figures S52 and S53). **6** had a redshifted CPL signal at 660 nm, with a g_{lum} of 0.003 (Figure S54).

Notably, the dynamic isomerization process of the largest BN-HNG molecule, **6**, was evaluated by DFT calculations at the B3-LYP-D3(BJ)/6-31G(d) level (Figure 7d). The energy barrier required for the transformation from (M_{bay}, M_{9H}, M_{bay})-**6** to (M_{bay}, M_{9H}, P_{bay})-**6** was 6.1 kcal/mol. The theoretical result was in good agreement with the results of variable-temperature NMR (VTNMR) experiments in CD_2Cl_2, whereas no splitting of signals was found even at 193 K (Figures S10 and S11).[29] The C_2-configuration (M_{bay}, M_{9H}, M_{bay}) was more stable than the (M_{bay}, M_{9H}, P_{bay}) isomer, which was confirmed by X-ray structure. The energy barrier for the transformation of (M_{bay}, M_{9H}, P_{bay})-**6** to (M_{bay}, P_{9H}, P_{bay})-**6** was increased to 57.9 kcal/mol owing to the congested [9]helicene. Similar to the pristine [9]helicene, a local minimum for (M_{bay}, LM_{9H}, P_{bay})-**6** of 48.2 kcal/mol was found. The high energy barrier of the multiple-step racemization process of **6** was confirmed by the unchanged CD spectra after heating (Figure S55). The concentration-dependent NMR experiment of **6** indicated self-aggregation at the 1–8 mM level, whereas no obvious segregation signal evolved in the CD spectra after serial dilution from 0.16 mM (Figure 8a). The difference in CD intensities indicated that **6** displayed monomeric properties at 10^{-5} M.

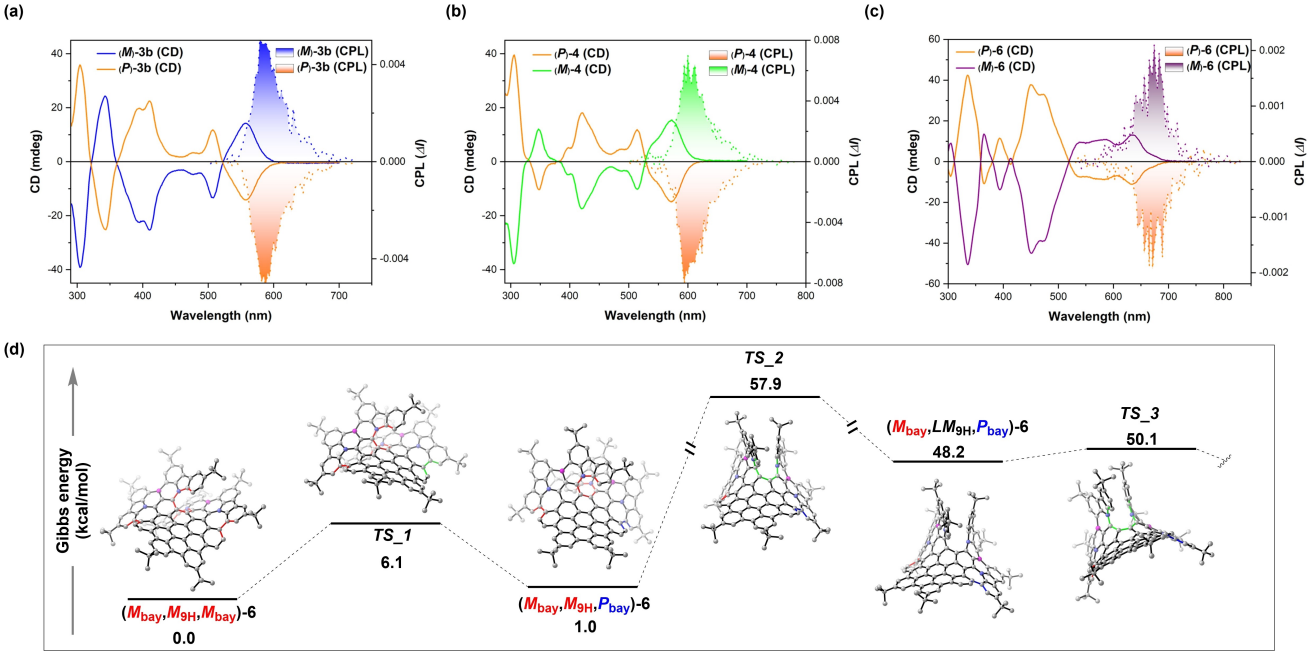

Figure 7. CD and CPL spectra of **3b** (a), **4** (b), and **6** (c). Calculated racemization process of **6** at B3LYP-D3(BJ)/6-31G(d) level of theory (d).

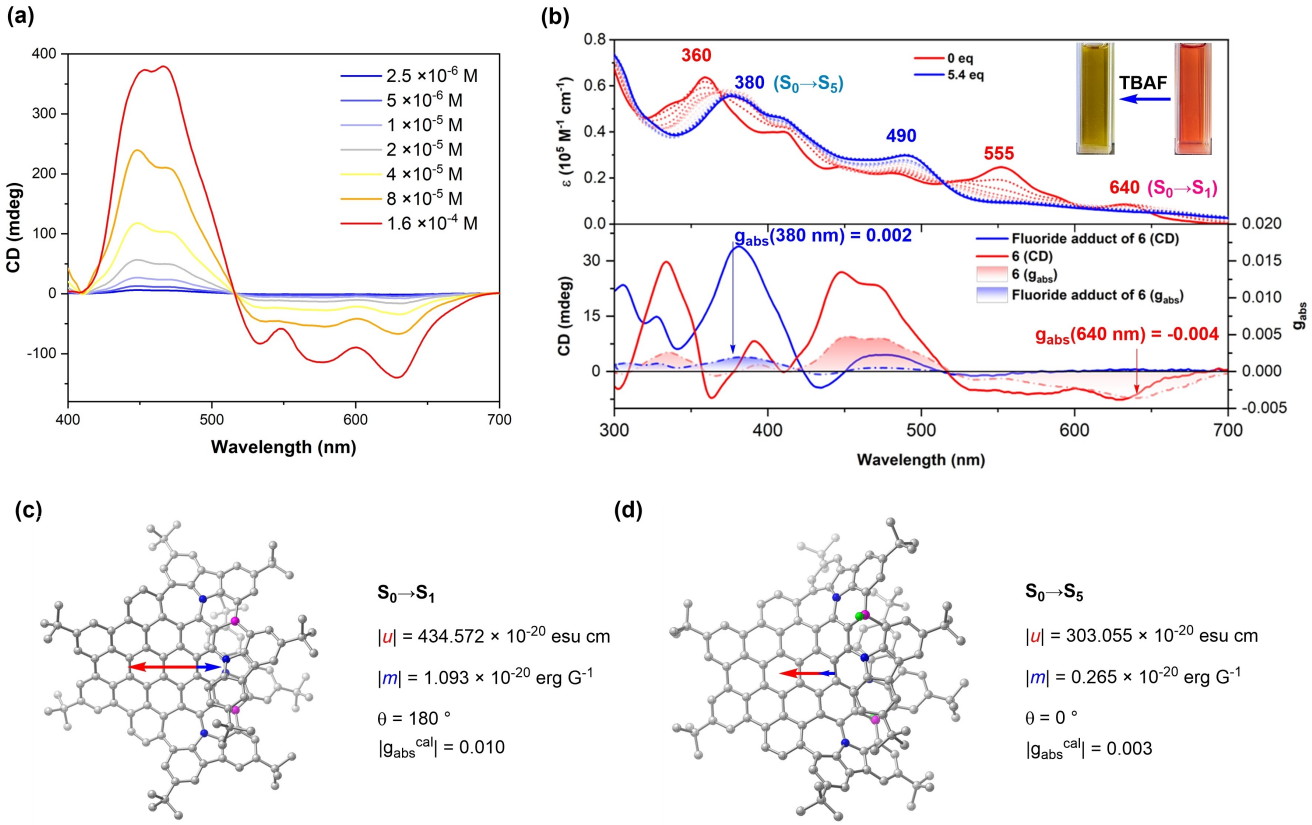

Figure 8. Variable-concentration CD spectra of (*P*)-**6** in toluene with serial dilutions from 1.6×10^{-4} M (a). Titration of (*P*)-**6** by TBAF monitored by UV/Vis spectra in toluene with increment of 0.3 eq. TBAF, and the corresponding CD spectra before (red) and after (blue) addition of 5.4 eq. TBAF (b). The inset shows the graph before and after addition of TBAF. Calculated transition dipole moments of **6** ($S_0 \rightarrow S_1$ transition, c) and the difluoride adduct **6-F** ($S_0 \rightarrow S_5$ transition, d) at PBE0/6-311G(d)/(SMD, toluene) level of theory. The magnetic transition dipole moments (blue arrows) were magnified for clarity.

To probe the chirality transfer of **6** upon coordination of fluoride anions, a titration experiment was conducted (Figure 8b). Similar to racemic **1**, when enantiomeric (*P*)-**6** was applied, the characteristic absorption peaks of **6** at 640, 555, and 360 nm gradually decreased, and peaks at 490 and 380 nm evolved. The corresponding CD spectrum of fluoride adduct of **6** was recorded, indicating a maximum g_{abs} at 380 nm for $S_0 \rightarrow S_5$ transition. The calculated $|g_{abs}|$ values of **6** (650 nm) and its difluoride adduct **6-F** (380 nm) at the PBE0/6-311G(d)/(SMD, toluene) level of theory were in accordance with the experimental results (Figures 8c and 8d).

Conclusion

In summary, we have disclosed a novel stepwise cyclodehydrogenative approach for modular synthesis of nonalternant B,N-embedded helical nanographenes with controllable integration of azepine units. Wide-range color tuning with narrow emission bands of these BN-HNGs was achieved, demonstrating the potential of this approach for systematic modulation of their photophysical and optoelectronic properties. Anion-responsive chiroptical properties were also established by the stereospecific coordination of fluoride to prochiral boron centers. Furthermore, the BN-HNGs showed structure-dependent packing behaviours. Stronger intermolecular π-π interactions were found for the BN-HNGs with increased π-surfaces. Especially, the newly formed azepine units resulted in a multiple-step dynamic racemization process with low barriers for the interconversion of bay regions, which was beneficial for conformational recognition to form chiral conglomerates. Finally, the large twisted C_2-symmetric π-surface and the dynamic chiral skeleton induced by curved azepines might have synergistic effects on self-recognition of enantiomers of **6** to achieve the intriguing spontaneous resolution behavior. Our study provides a promising bottom-up synthetic approach towards nonalternant nanocarbon-based materials, such as chiral liquid crystals, combing tunable chiroptical properties and assembly behaviors of BN-HNGs.

Acknowledgements

This work was supported by the Hong Kong Research Grants Council (27301720, 17304021, 17309023), National Natural Science Foundation of China (22122114). J.L. is

grateful for the funding from The University of Hong Kong (HKU) and ITC to the SKL. We acknowledge the computer cluster (HPC2021) of HKU and the support from Hong Kong Quantum AI Lab Limited. We thank the UGC funding administered by HKU for supporting the Time-of-Flight Mass Spectrometry Facilities under the Support for Interdisciplinary Research in Chemical Science. The authors thank Ms. Bonnie Yan at Department of Chemistry of HKU for assistance with VT NMR experiments. The authors thank Dr. Wenzheng Fan at Shanghai Institute of Organic Chemistry for helpful discussions.

Conflict of Interest

The authors declare no conflict of interest.

Data Availability Statement

The data that support the findings of this study are available in the supplementary material of this article.

Keywords: Boron-nitrogen · Helical nanographene · Negative curvature · Scholl reaction · Spontaneous resolution

[1] a) J. Crassous, I. G. Stará, I. Starý, Eds. *Helicenes: Synthesis, Properties and Applications.* Wiley-VCH, Weinheim, **2022**; b) Y. Shen, C.-F. Chen, *Chem. Rev.* **2012**, *112*, 1463–1535; c) T. Mori, *Chem. Rev.* **2021**, *121*, 2373–2412; d) Y. Zhu, J. Wang, *Acc. Chem. Res.* **2023**, *56*, 363–373.

[2] a) B. P. Bloom, Y. Paltiel, R. Naaman, D. H. Waldeck, *Chem. Rev.* **2024**, *124*, 1950–1991; b) R. Rodriguez, C. Naranjo, A. Kumar, P. Matozzo, T. K. Das, Q. Zhu, N. Vanthuyne, R. Gomez, R. Naaman, L. Sanchez, J. Crassous, *J. Am. Chem. Soc.* **2022**, *144*, 7709–7719; c) M. Kettner, V. V. Maslyuk, D. Nürenberg, J. Seibel, R. Gutierrez, G. Cuniberti, K.-H. Ernst, H. Zacharias, *J. Phys. Chem. Lett.* **2018**, *9*, 2025–2030.

[3] a) M. Gingras, *Chem. Soc. Rev.* **2013**, *42*, 1051–1095; b) J. R. Brandt, F. Salerno, M. J. Fuchter, *Nat. Chem. Rev.* **2017**, *1*, 0045.

[4] a) S. H. Pun, Q. Miao, *Acc. Chem. Res.* **2018**, *51*, 1630–1642; b) J. M. Fernández-García, P. Izquierdo-García, M. Buendía, S. Filippone, N. Martín, *Chem. Commun.* **2022**, *58*, 2634–2645; c) Chaolumen, I. A. Stepek, K. E. Yamada, H. Ito, K. Itami, *Angew. Chem. Int. Ed.* **2021**, *60*, 23508–23532; d) Y. Fei, J. Liu, *Adv. Sci.* **2022**, *9*, 2201000.

[5] a) L. Yang, Y.-Y. Ju, M. A. Medel, Y. Fu, H. Komber, E. Dmitrieva, J.-J. Zhang, S. Obermann, A. G. Campaña, J. Ma, X. Feng, *Angew. Chem. Int. Ed.* **2023**, *62*, e202216193; b) A. K. Swain, K. Kolanji, C. Stapper, P. Ravat, *Org. Lett.* **2021**, *23*, 1339–1343; c) A. Swain, P. Ravat, P. Org, *Chem. Front.* **2023**, *10*, 3714–3725.

[6] M. A. Medel, R. Tapia, V. Blanco, D. Miguel, S. P. Morcillo, A. G. Campaña, *Angew. Chem. Int. Ed.* **2021**, *60*, 6094–6100.

[7] M. A. Medel, C. M. Cruz, D. Miguel, V. Blanco, S. P. Morcillo, A. G. Campaña, *Angew. Chem. Int. Ed.* **2021**, *60*, 22051–22056.

[8] Y. Zhang, S. H. Pun, Q. Miao, *Chem. Rev.* **2022**, *122*, 14554–14593.

[9] a) E. Yashima, N. Ousaka, D. Taura, K. Shimomura, T. Ikai, K. Maeda, *Chem. Rev.* **2016**, *116*, 13752–13990; b) J. A. Schmidt, E. H. Wolpert, G. M. Sparrow, E. R. Johnson, K. E. Jelfs, *Cryst. Growth Des.* **2023**, *23*, 8909–8917; c) K. Kato, K. Takaba, S. Maki-Yonekura, N. Mitoma, Y. Nakanishi, T. Nishihara, T. Hatakeyama, T. Kawada, Y. Hijikata, J. Pirillo, L. T. Scott, K. Yonekura, Y. Segawa, K. Itami, *J. Am. Chem. Soc.* **2021**, *143*, 5465–5469.

[10] F. Gan, G. Zhang, J. Liang, C. Shen, H. Qiu, *Angew. Chem. Int. Ed.* **2024**, *63*, e202320076.

[11] a) C. Duan, J. Zhang, J. Xiang, X. Yang, X. Gao, *Angew. Chem. Int. Ed.* **2022**, *61*, e202201494; b) G. M. Upadhyay, H. M. Mande, D. K. Pithadia, R. H. Maradiya, A. V. Bedekar, *Cryst. Growth Des.* **2019**, *19*, 5354–5361; c) K. Mori, T. Murase, M. Fujita, *Angew. Chem. Int. Ed.* **2015**, *54*, 6847–6851; d) P. J. Evans, J. Ouyang, L. Favereau, J. Crassous, I. Fernández, J. Perles, N. Martín, *Angew. Chem. Int. Ed.* **2018**, *57*, 6774–6779.

[12] a) K. Dhbaibi, L. Favereau, J. Crassous, *Chem. Rev.* **2019**, *119*, 8846–8953; b) J.-K. Li, X.-Y. Chen, Y.-L. Guo, X.-C. Wang, A. C.-H. Sue, X.-Y. Cao, X.-Y. Wang, *J. Am. Chem. Soc.* **2021**, *143*, 17958–17963; c) X. Wu, J.-W. Huang, B.-K. Su, S. Wang, L. Yuan, W.-Q. Zheng, H. Zhang, Y.-X. Zheng, W. Zhu, P.-T. Chou, *Adv. Mater.* **2022**, *34*, 2105080; d) F. Zhang, F. Rauch, A. Swain, T. B. Marder, P. Ravat, *Angew. Chem. Int. Ed.* **2023**, *62*, e202218965; e) Q. Wang, L. Yuan, C. Qu, T. Huang, X. Song, Y. Xu, Y.-X. Zheng, Y. Wang, *Adv. Mater.* **2023**, *35*, 2305125; f) Y. Yang, N. Li, J. Miao, X. Cao, A. Ying, K. Pan, X. Lv, F. Ni, Z. Huang, S. Gong, C. Yang, *Angew. Chem. Int. Ed.* **2022**, *61*, e202202227; g) Y. Xu, Q. Wang, X. Cai, C. Li, Y. Wang, *Adv. Mater.* **2021**, *33*, 2100652; h) Z.-P. Yan, L. Yuan, Y. Zhang, M.-X. Mao, X.-J. Liao, H.-X. Ni, Z.-H. Wang, Z. An, Y.-X. Zheng, J.-L. Zuo, *Adv. Mater.* **2022**, *34*, 2204253; i) X.-J. Liao, D. Pu, L. Yuan, J. Tong, S. Xing, Z.-L. Tu, J.-L. Zuo, W.-H. Zheng, Y.-X. Zheng, *Angew. Chem. Int. Ed.* **2023**, *62*, e202217045.

[13] a) T. Hatakeyama, K. Shiren, K. Nakajima, S. Nomura, S. Nakatsuka, K. Kinoshita, J. Ni, Y. Ono, T. Ikuta, *Adv. Mater.* **2016**, *28*, 2777–2781; b) B. Lei, Z. Huang, S. Li, J. Liu, Z. Bin, J. You, *Angew. Chem. Int. Ed.* **2023**, *62*, e202218405; c) M. Mamada, A. Aoyama, R. Uchida, J. Ochi, S. Oda, Y. Kondo, M. Kondo, T. Hatakeyama, *Adv. Mater.* **2024**, *36*, 2402905.

[14] During the preparation of this manuscript, Li and Chen et al. reported the relevant compound (**1**) as a yellow emitter showing highly efficient circularly polarized electroluminescence (Published on 21 February). However, the nitrogen-bridged [9]helicene (**2**) and the stepwise lateral π-extension of **1** via selective Scholl reaction establish a robust synthetic strategy toward BN-HNGs, which distinguishes the current work form their contribution. See: W.-C. Guo, W.-L. Zhao, K.-K. Tan, M. Li, C.-F. Chen, *Angew. Chem. Int. Ed.* **2024**, *63*, e202401835.

[15] M. Buendía, J. M. Fernández-García, J. Perles, S. Filippone, N. Martín, *Nat. Synth.* **2024**, *3*, 545–553.

[16] Deposition numbers 2309907 (for **1**), 2309911 (for **1-F**), 2335063 (for **2**), 2335064 (for **2/TCNB**), 2309909 (for **3a**), 2334722 (for **4**), 2352136 (for **5**), and 2334723, 2334724 (for **6**) contain the supplementary crystallographic data for this paper. These data are provided free of charge by the joint Cambridge Crystallographic Data Centre and Fachinformationszentrum Karlsruhe Access Structures service.

[17] a) J. Ma, Y. Fu, E. Dmitrieva, F. Liu, H. Komber, F. Hennersdorf, A. A. Popov, J. J. Weigand, J. Liu, X. Feng, *Angew. Chem. Int. Ed.* **2020**, *59*, 5637–5642; b) J. Wang, C. Shen, G. Zhang, F. Gan, Y. Ding, H. Qiu, *Angew. Chem. Int. Ed.* **2022**, *61*, e202115979; c) Z. Qiu, S. Asako, Y. Hu, C.-W. Ju, T. Liu, L. Rondin, D. Schollmeyer, J.-S. Lauret, K. Müllen, A. Narita, *J. Am. Chem. Soc.* **2020**, *142*, 14814–14819.

[18] D. Hellwinkel, T. Kistenmacher, *Liebigs Ann. Chem.* **1989**, 945–949.

[19] A. Loudet, K. Burgess, *Chem. Rev.* **2007**, *107*, 4891–4932.

[20] D. Tan, J. Dong, T. Ma, Q. Feng, S. Wang, D.-T. Yang, *Angew. Chem. Int. Ed.* **2023**, *62*, e202304711.
[21] X. Li, G. Zhang, Q. Song, *Chem. Commun.* **2023**, *59*, 3812–3820.
[22] K. Matsumoto, U. Harinaga, R. Tanaka, A. Koyama, R. Hagiwara, K. Tsunashima, *Phys. Chem. Chem. Phys.* **2014**, *16*, 23616–23626.
[23] a) G. E. M. Crisenza, D. Mazzarella, P. Melchiorre, *J. Am. Chem. Soc.* **2020**, *142*, 5461–5476; b) K. P. Goetz, D. Vermeulen, M. E. Payne, C. Kloc, L. E. McNeil, O. D. Jurchescu, *J. Mater. Chem. C* **2014**, *2*, 3065–3076.
[24] Y. Chen, C. Lin, Z. Luo, Z. Yin, H. Shi, Y. Zhu, J. Wang, *Angew. Chem. Int. Ed.* **2021**, *60*, 7796–7801.
[25] Y. Zou, Y. Han, S. Wu, X. Hou, C. H. E. Chow, J. Wu, *Angew. Chem. Int. Ed.* **2021**, *60*, 17654–17663.
[26] a) D. J. Gregg, C. M. A. Ollagnier, C. M. Fitchett, S. M. Draper, *Chem. Eur. J.* **2006**, *12*, 3043–3052; b) X. Dou, X. Yang, G. J. Bodwell, M. Wagner, V. Enkelmann, K. Müllen, *Org. Lett.* **2007**, *9*, 2485–2488.
[27] T. Lu, F. Chen, *J. Comput. Chem.* **2012**, *33*, 580–592.
[28] Y.-Y. Ju, H. Luo, Z.-J. Li, B.-H. Zheng, J.-F. Xing, X.-W. Chen, L.-X. Huang, G.-H. Nie, B. Zhang, J. Liu, Y.-Z. Tan, *Angew. Chem. Int. Ed.* **2024**, *63*, e202402621.
[29] Y. Wang, A. D. Stretton, M. C. McConnell, P. A. Wood, S. Parsons, J. B. Henry, A. R. Mount, T. H. Galow, *J. Am. Chem. Soc.* **2007**, *129*, 13193–13200.

Manuscript received: April 5, 2024
Accepted manuscript online: July 19, 2024
Version of record online: September 12, 2024